

THE EFFECT OF CIRCULAR OPENINGS ON THE BRITTLE-DUCTILE FRACTURE OF FERROUS FLAT BARS

Shariyar Beizaee[†], Kaspar Willam^{†*} and Giovanna Xotta[†]

[†]Department of Civil and Environmental Engineering, University of Houston
Cullen College of Engineering, N107 Engineering Building 1, Houston TX 77204
e-mail: kwillam@central.uh.edu, sbeizaee@uh.edu, gxotta@uh.edu

Key words: Tension Tests on Flat Bars with Circular Holes, Digital Image Correlation Analysis, Finite Element Formulations of Brittle and Ductile Fracture.

Abstract. The stress distribution in the vicinity of circular perforations has been studied by Kirsch over a century ago [1]. Inglis extended the analysis of circular openings to elliptical holes [4] which subsequently led to the development of linear elastic and nonlinear inelastic fracture mechanics.

This paper revisits the fundamentals of elastic stress concentrations in the proximity of circular perforations of different diameters and presents results of an experimental series on ferrous flat bars made of high strength steel, mild steel and cast iron. Focus is the issue whether strain hardening and localized yielding emanating from the stress concentrations at the circular perforation explain the puzzling effect described by Kirsch that the ultimate load capacity of the perforated bars increase rather than decrease and definitely not by a factor of three as expected for brittle materials when compared to the non-perforated bars.

A newly acquired digital image correlation system sheds additional light on the development of plastic zones and shear bands beyond the original area reduction measurements by Kirsch. Elastoplastic finite element simulations complement the digital image analysis with field data from computational simulations of plasticity models for brittle and ductile fracture. The paper concludes with remarks on the effect of ductility on the mode of failure, the reduction of strength due to the opening, and the load ratio of perforated over non-perforated specimens.

1 INTRODUCTION

According to the St Venant principle the axial stress σ_{axial} in a flat tension specimen is uniformly distributed sufficiently far away from the loading grips. Geometric changes in the cross section cause loss of uniformity and result in stress concentrations which are considerably larger than the nominal axial stress of the un-notched section. In his seminal paper Kirsch [1898] presented the linear elastic stress distribution at a point P in the vicinity of a circular perforation in form of Equation 1 [5] using polar coordinates (r, θ) . In the case of a finite flat bars the stress concentration factor diagrams

are widely reported in elementary mechanics of materials text books. They all show that the stress concentration factor tends to three as the hole diameter decreases and that the factor approaches two as the hole diameter increases.

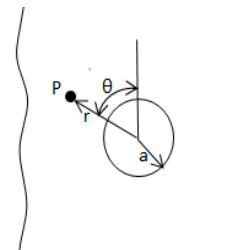


Figure 1: Schematic of a hole in an infinite plate

$$\begin{aligned}
 \sigma_{rr} &= \frac{\sigma}{2} \left(1 - \frac{a^2}{r^2}\right) + \frac{\sigma}{2} \left(1 - \frac{a^2}{r^2}\right) \left(1 - \frac{3a^2}{r^2}\right) \cos(2\theta) \\
 \sigma_{\theta\theta} &= \frac{\sigma}{2} \left(1 + \frac{a^2}{r^2}\right) - \frac{\sigma}{2} \left(1 + \frac{3a^4}{r^4}\right) \cos(2\theta) \\
 \sigma_{r\theta} &= -\frac{\sigma}{2} \left(1 - \frac{a^2}{r^2}\right) \left(1 + \frac{3a^2}{r^2}\right) \sin(2\theta)
 \end{aligned} \quad (1)$$

Starting point of the Kirsch solution was the linear elastic result of an infinite panel with a circular hole under uniform tension in the far field. It should be noted that the classical stress concentration factor of three was re-evaluated with higher order continuum theories and gradient elasticity theories resulting in a significant reduction of the classical stress concentration factor three to values close to two.

$$\begin{aligned}
 \sigma_{rr} &= \sigma \left(1 + \frac{a^2}{r^2}\right) \\
 \sigma_{\theta\theta} &= \sigma \left(1 - \frac{a^2}{r^2}\right)
 \end{aligned} \quad (2)$$

Aside from the analytical stress concentration results of linear elasticity, Kirsch [1] presented in his paper the results of a series of experiments on cast iron and mild steel flat bars ('Gusseisen und Flusseisen') with circular perforations of different diameters in order to illustrate the effect of the hole size on the ultimate load bearing capacity and tensile strength of cast iron and mild steel. His experimental results are summarized in figure 2 which depicts the reduction of load capacity with hole diameter size normalized by the load capacity of the unperforated bar and the nominal width of the bar without perforation. Based on the linear elastic solution of equation 1 he expected to see an elastic stress concentration factor of three at the edge of the circular hole for the cast iron flat bar. However his experimental observations on cast iron flat bars showed a reduction of the load capacity of less the 0.9. In fact, figure 2 depicts the experimental observations of Kirsch in form of the ultimate load capacity of the perforated over non-perforated specimen, indicating less than fifteen percent reduction in contradiction to the linear elasticity solution governing brittle fracture.

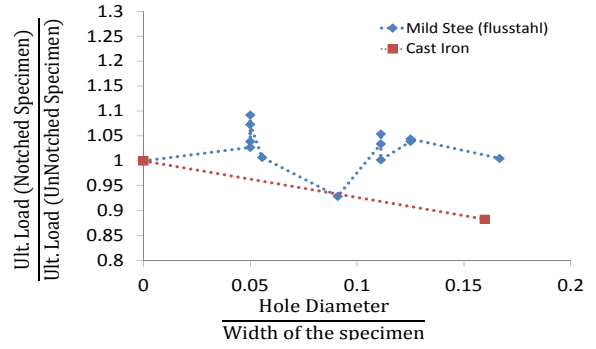


Figure 2: Load ratio with respect to nominal hole diameter of Kirsch experiments

This raises the question whether strain hardening, localized yielding and plastic deformations may explain this contradictory behavior.

In the case of mild steel, the experimental results of Kirsch exhibit no notch sensitivity of the load bearing capacity of the test specimen which can be explained by the high ductility and plastic redistribution capacity of the material due to hardening in the region near the stress concentrations at the lateral edges of the circular perforation.

2 EXPERIMENTAL OBSERVATIONS

A set of experiments was performed on flat bars with circular perforations. In order to study the effect of perforation and stress concentration on the mode of failure and elastoplastic localization.

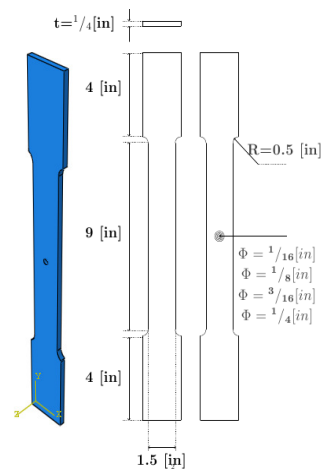


Figure 3: Dimensions of the flat bars

The specimens were made from cast iron, mild steel and high strength steel while the dimensions of the specimens depicted in figure 3 had the same geometry as the test articles used by Kirsch. There were ten coupons tested for each material type and duplicate coupons for each hole diameter, the hole diameters are $1/16$, $1/8$, $3/16$ and $1/4$ of an inch.

The flat bars were tested under uniaxial tension using displacement control and the rate of the displacement controlled tests was kept the same for all test samples in order to eliminate possible strain rate effects. The tension test was performed on a Tinius Olsen test frame of 340 kip axial capacity and the data was collected using data acquisition for axial LVDT measurements and a newly acquired Digital Image Correlation (DIC) system.

2.1 Experiment results

The corresponding load deformation curves of the axial tension tests are depicted in figure 4.

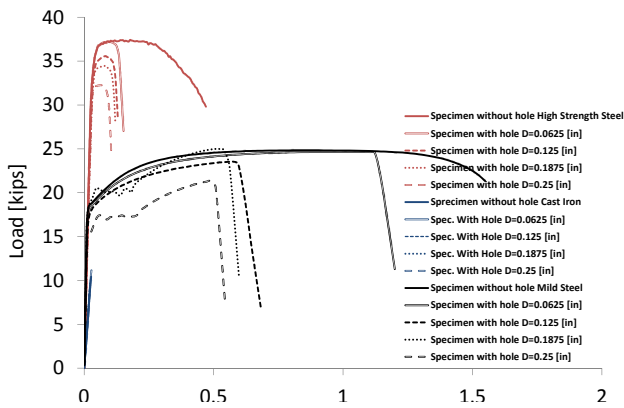


Figure 4: Load deformation curves of uniaxial tension tests

The test data in figure 4 showed that the ultimate load capacity of high strength steel specimens decreased as the hole diameter increased. while mild steel and cast iron specimens did exhibit fluctuations in load capacity based on the hole diameter. The summary results are depicted in figures 5 and 6 showing the ultimate load capacity of notched over un-notched specimen with regards to nominal hole diameter and

the ultimate nominal stress of notched specimen at the perforated ligament over that of the un-notched specimen.

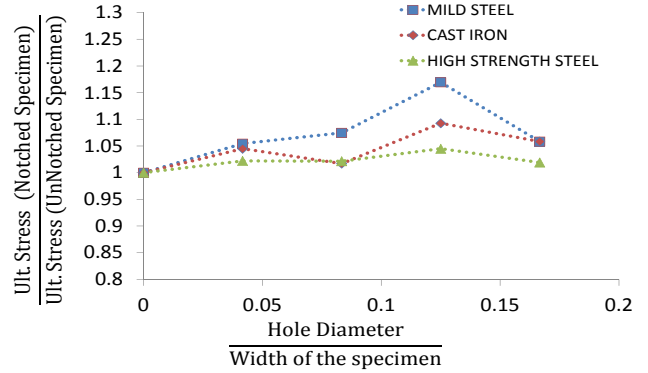


Figure 5: Ultimate load ratio

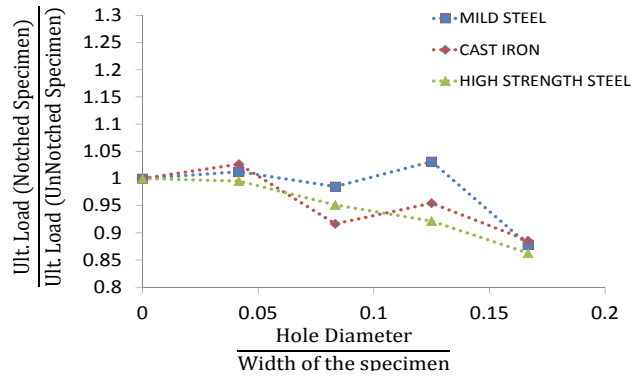


Figure 6: Ultimate nominal stress ratio

2.2 Failure mechanisms

The failure and fracture mechanisms in metals is divided into three types, ductile fracture, cleavage and inter-granular fracture from which the first two are the most common types.

Ductile failure has three stages which are formation of a free surface at an inclusion or a second phase material, void growth because of hydrostatic stress or plastic strain and void coalescence with the neighborhood void. Void nucleation and coalescence are the main failure mechanisms at the center of the specimen because of the higher density of the voids and because of the triaxiality of the stress. However close to the free edges, the density of the voids

decreases and shear failure becomes the dominant failure pattern. This describes the failure mechanism of mild steel specimen without perforation, figure 7.



Figure 7: Failure mechanism of mild steel

It should be noted that if cylindrical tension specimens were used, a cup-cone failure pattern would have been observed, but since flat bars were used of significant thickness ($t = 0.25[in]$), the failure pattern is a shear dominant failure mechanism through the thickness depicted in Figure 8.

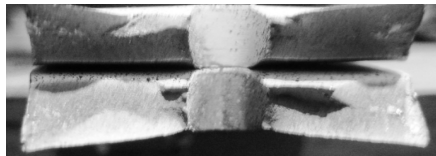


Figure 8: In depth failure mechanism of mild steel

In the case of ductile fracture of the perforated specimens the cracks tended to grow in the direction of maximum plastic strain, while the global geometry constraints required the crack to remain in-plane. Consequently, in order to satisfy both requirements the crack grew in a zig-zag pattern [6] resulting a cleavage failure mechanism of the core material.

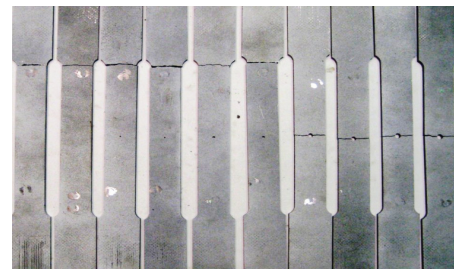
Cleavage fracture results in rapid propagation of crack in a trans-granular pattern. This is the most common fracture pattern for brittle metals but it should be noted that it can be preceded by ductile crack growth and plastic behavior. This type of failure is oriented perpendicular to the direction of maximum principal stress. This mechanism is characteristic for the

failure behavior of cast iron as can be seen in Figure 9.

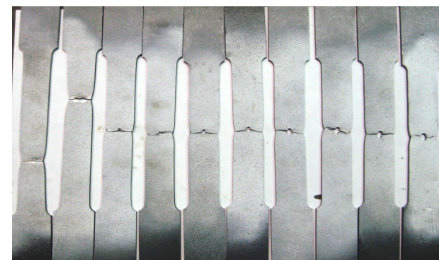


Figure 9: Failure mechanism of cast iron

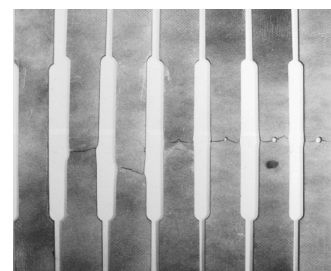
The failure patterns of perforated mild steel bars made of cast iron and high strength steel were tested at the University of Houston are shown in Figure 10.



(a) Cast iron



(b) Mild steel



(c) High Strength Steel

Figure 10: Failure pattern of the tested specimens

Note, all cast iron specimens failed in form of a cleavage mechanism and unstable crack

growth pattern, while the mild steel and high strength steel specimens failed in a ductile manner with necking in the center region, shear lips close to the edges and through-depth shear dominant failure. Some of the specimens showed a zig-zag failure pattern.

2.3 DIC observations

The strain field and deformations of the flat bars were captured and analyzed using the Digital Image Correlation system. This photogrammetric non-contact device was mounted in front of the painted sample for continuous recording the relative movement of black dots on the white specimen during deformation. ARAMIS software of the GOM instrument displayed images of the displacement and strain fields. In order to verify the displacement readings, the axial extensions of the cast iron experiments were compared with LVDT results and the root mean square deviation was calculated. The results of this comparison is tabulated in Table 1 showing less deviation than one hundredth of the specimen elongation LVDT measurement which is the precision of the DIC technology.

Table 1: Root mean square deviation

$\Phi[in]$	0	$1/16$	$1/8$	$3/16$	$1/4$
RMSD [in]	5E-4	4.8E-4	5.7E-4	2.4E-4	4E-4

The Mises strain distribution of the mild steel specimens close to the failure stage is shown in Figure 11. The shear bands are clearly visible in these images for specimens with holes while significant necking was observed in the non-perforated specimens. The magnitude of the axial strain at the edges of the hole is in the range of 35% and is large in comparison to the far field strain. This explains the plastification caused by the circumferential stress concentration. It is interesting to note that the axial plastic strains in the non-perforated specimens did exhibit even larger values of up to 70% in the localized shear zones, see Figure 12.

The DIC results for cast iron show a much smaller increase of strain at the edge of the circular perforation with no shear bands which confirms that cast iron exhibits brittle failure, see Figure 13.

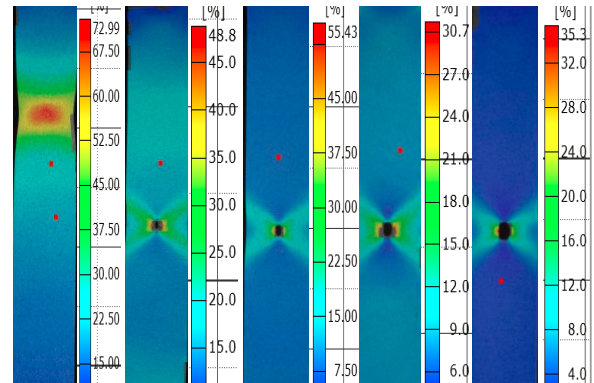


Figure 11: Mises strain distribution on mild steel specimens

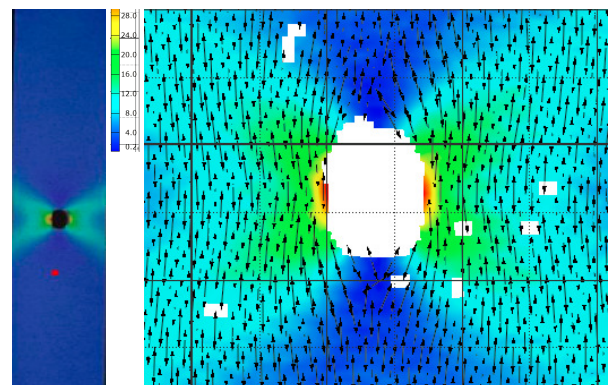


Figure 12: Principal strain direction in the vicinity of the hole

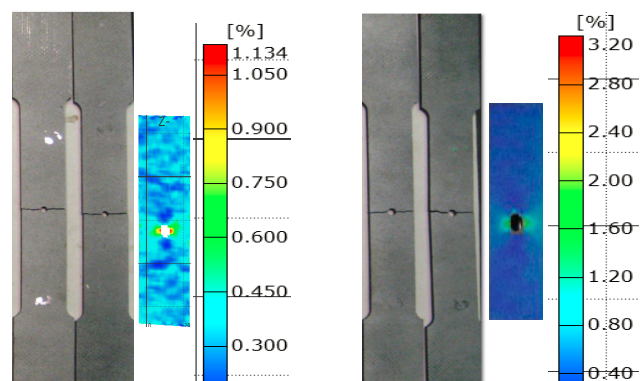


Figure 13: Mises strain distribution on cast iron specimens

3 Finite Element Simulations

Finite element models were used to model the behavior of mild steel and cast iron flat bars. To this end, a linear elastic, isotropic hardening-softening J_2 plasticity model was used for mild steel using best fit of the experimental load-deformation of the unnotched specimens. A maximum principal stress damage model was used for cast iron with a very steep softening slope for brittle failure.

3.1 J2 plasticity

Appropriate constitutive relations may be cast in form of a local material format of entropy inequality and elasticity. Omitting thermal fields due to the slow nature of the tension test, it suffices to consider only the mechanical part of the total dissipation. Considering the free energy density as $\Psi = \Psi[\epsilon, \underline{q}]$ and using the entropy inequality, the pertinent constitutive relations for elastic and dissipative stresses are established as follow.

$$(D_0)_{\text{mech}} = \sigma : \epsilon^p + \underline{Q}^T \cdot \underline{\dot{q}} \geq 0 \quad (3)$$

where \underline{q} denotes the set of internal variables. The free energy function for the linear elasticity and isotropic hardening is described in Equation 4 where the elastic and plastic parts are decomposed additively.

$$\begin{aligned} \Psi &= \Psi_{\text{elastic}}[\epsilon] + \Psi_{\text{plastic}}[\kappa] \\ &= \frac{1}{2} \epsilon : \mathbf{E} : \epsilon + \frac{1}{2} H \kappa^2 \end{aligned} \quad (4)$$

From the free energy function the stress and hardening variable are as follow

$$\begin{aligned} \sigma &= \frac{\partial \Psi}{\partial \epsilon} = \mathbf{E} : \epsilon \\ K &= \frac{\partial \Psi}{\partial \kappa} = H \kappa \end{aligned} \quad (5)$$

The yield function of von Mises is used for the case of mild steel and high strength steel in the form,

$$F = \sqrt{3J_2} - (\sigma_y + K) \quad (6)$$

The plastic multiplier is calculated based on Prager's consistency condition and is formulated as

$$\dot{\lambda} = \frac{\mathbf{n} : \mathbf{E} : \dot{\epsilon}}{\mathbf{n} : \mathbf{E} : \mathbf{n} + H} \quad (7)$$

where \mathbf{n} is the gradient of the yield function with respect to stress tensor or in geometrical terms the normal to the yield surface. Assuming associated plastic flow, the plastic potential function is the same as the yield function and their gradients are the same.

The plastic flow rule and the internal variable rate are for isotropic hardening,

$$\begin{aligned} \dot{\epsilon}^P &= \dot{\lambda} \mathbf{n} \\ \dot{\kappa} &= \dot{\lambda} \end{aligned} \quad (8)$$

The elastoplastic tangent operator may be assembled in the differential format as follows,

$$\begin{aligned} \mathbf{E}_{ep} &= \mathbf{E} - \frac{1}{h} \mathbf{E} : \mathbf{n} \otimes \mathbf{n} : \mathbf{E} \\ h &= \mathbf{n} : \mathbf{E} : \mathbf{n} + H \end{aligned} \quad (9)$$

In order to minimize the hardening/softening error, the elastoplastic formulations are extended to a quadrilinear form with H_1 , H_2 and H_3 which denote the piecewise constant hardening parameters. The constitutive model was written in Fortran and was implemented in Abaqus using the UMAT subroutine to integrate material models. The quadrilinear hardening/softening model was calibrated with the load-deformation curve of non-perforated mild steel specimen. The comparison of the Abaqus model with the experimental data is depicted in Figure 14 for verification.

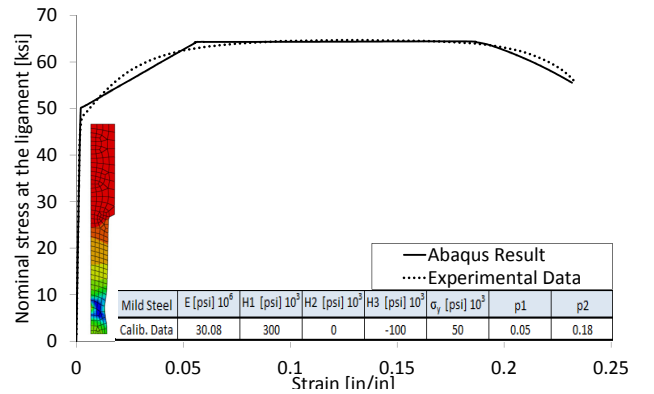


Figure 14: Calibrated model and parameters

3.2 Localization analysis

While diffuse failure refers to a material instability and zero or negative values of the second order work density, localized failure in form of weak discontinuities reflect formation

of jumps of the strain rates across emerging discontinuity surfaces. The localization is caused by the jump of velocity gradients across the discontinuity surface in Equation 10. Thereby the velocity field is assumed to remain C_0 continuous.

$$\begin{aligned} [[\dot{\mathbf{u}}]] &= \dot{\mathbf{u}}^+ - \dot{\mathbf{u}}^- = \mathbf{0} \\ [[\nabla\dot{\mathbf{u}}]] &= \nabla\dot{\mathbf{u}}^+ - \nabla\dot{\mathbf{u}}^- \neq \mathbf{0} \end{aligned} \quad (10)$$

The '+' and '-' signs refer to the positive and negative sides of the discontinuity surface. In order to satisfy the Maxwell compatibility condition, the jump in the velocity field should have the form

$$[[\nabla\dot{\mathbf{u}}]] = \dot{\gamma}\mathbf{M} \otimes \mathbf{N} \quad (11)$$

where \mathbf{N} is the normal to the localization surface and \mathbf{M} is the polarization vector. In the case that \mathbf{N} is equal to \mathbf{M} the localized failure is mode I or opening and when \mathbf{N} is perpendicular to \mathbf{M} is mode II or shear. The discontinuity in the strain rate field is defined as,

$$[[\dot{\boldsymbol{\epsilon}}]] = [[\nabla\dot{\mathbf{u}}]] = \frac{1}{2}\dot{\gamma}(\mathbf{M} \otimes \mathbf{N} + \mathbf{N} \otimes \mathbf{M}) \quad (12)$$

According to Cauchy's lemma the traction rate remains continuous across the discontinuity surface which leads to the localization condition as follows,

$$\mathbf{M} \cdot \mathbf{Q}_{ep} \cdot \mathbf{M} = 0 \quad (13)$$

where \mathbf{Q}_{ep} is the elastoplastic second order localization tensor as follows.

$$\begin{aligned} \mathbf{Q}_{ep} &= \mathbf{N} \cdot \mathbf{E}_{ep} \cdot \mathbf{N} \\ \mathbf{Q} &= \mathbf{N} \cdot \mathbf{E} \cdot \mathbf{N} \end{aligned} \quad (14)$$

For in-plane 2D finite element analysis, the localization direction may be stipulated in plane stress or plane strain. In the case of plane stress and uniaxial tension, the critical localization angle is $\theta_{crit} = 35.26^\circ$ and for plane strain it is $\theta_{crit} = 45^\circ$. So it is expected to see a 35.26° localization direction in the case of mild steel and high strength steel specimens. For the case of plane stress and plane strain the directional properties of the elastoplastic over elastic localization tensors are plotted for in Figure 15.

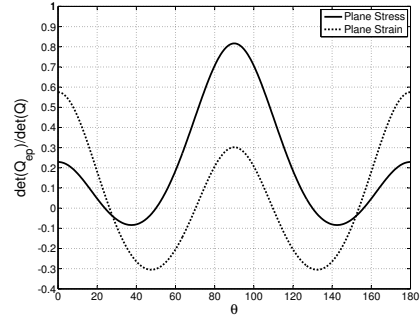


Figure 15: Elastoplastic localization study

3.3 Maximum principal stress damage model

The material parameters of cast iron are calibrated based on the non-perforate load-deformation curve which is depicted in Figure 16.

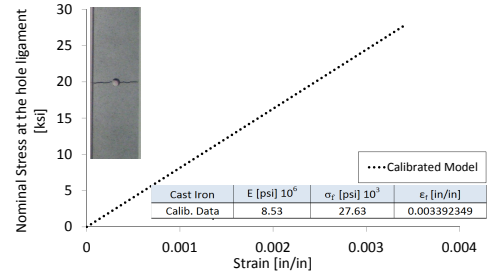


Figure 16: Cast iron calibration data

Based on the calibrated data, a linear elastic with maximum principal stress damage model was implemented in Abaqus in order to model the behavior of the perforated flat bar in uniaxial tension. In order to adequately model the behavior of cast iron and crack trajectory, the XFEM capability of Abaqus was activated and incorporated in the finite element model using Rankine's condition of maximum tensile stress for crack initiation and crack extension.

In classical finite elements a crack are required to follow inter element boundaries when remeshing is to be avoided. In contrast in XFEM this is no longer required since the

method adds additional degrees of freedom to the nodes of the elements intersected by the crack without changing the discretization. Therefore a single mesh is adequate to capture any crack path and length. The nodes of the elements that contain the crack tips are enriched by eight additional degrees of freedom, four degrees of freedom of the crack tip function for each Cartesian direction, and the nodes of the elements that contain the crack are enriched by two additional Heaviside functions multiplied by the element shape functions.

$$\mathbf{u}_{xfem}(\mathbf{x}) = \sum_i N_i(\mathbf{x})\mathbf{u}_i + \sum_i N_i(\mathbf{x})H(\mathbf{x})\mathbf{a}_i + \sum_i \left[N_i(\mathbf{x}) \sum_{\alpha=1}^4 F_{\alpha}(\mathbf{x})\mathbf{b}_{i\alpha} \right] \quad (15)$$

3.4 Results

The calibrated model for the non-perforated tension test is compared with the test results of the specimen with the hole diameter equal to a quarter of an inch. The comparison of the load-deformation data for mild steel and cast iron specimens are depicted in Figures 17 and 18.

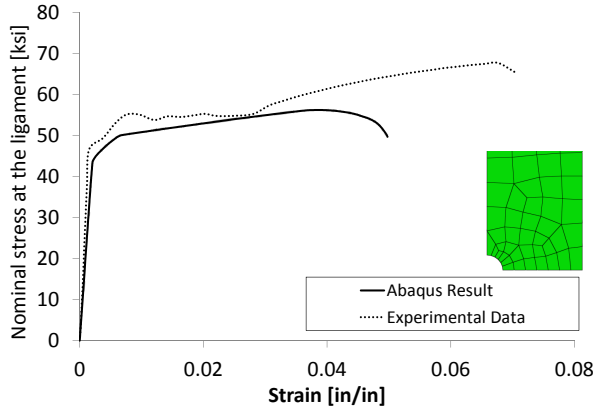


Figure 17: Comparison of the calibrated model with experimental data, mild steel

Using the calibration of the unnotched specimen, the finite element analysis of a quarter of a mild steel specimen was performed for different hole sizes. The axial plastic strain distribution and axial stress distribution in the vicinity of the

perforation are plotted and compared in Figures 19 and 20 consequently.

From these figures, the plastic field for mild steel exhibits an inclined failure mode direction that confirms the observations of DIC, in close agreement with the localization direction for plane stress due in spite of the finite thickness of the flat bar.

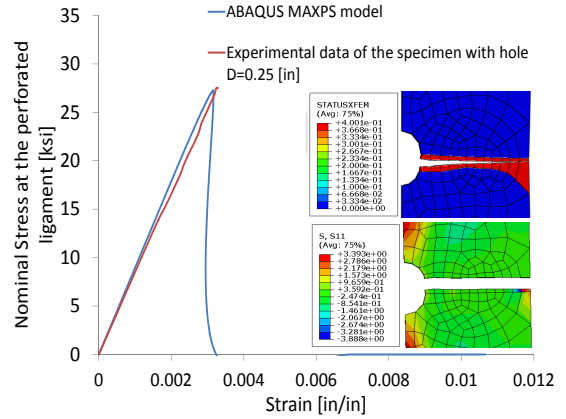


Figure 18: Comparison of the calibrated model with experimental data, cast iron

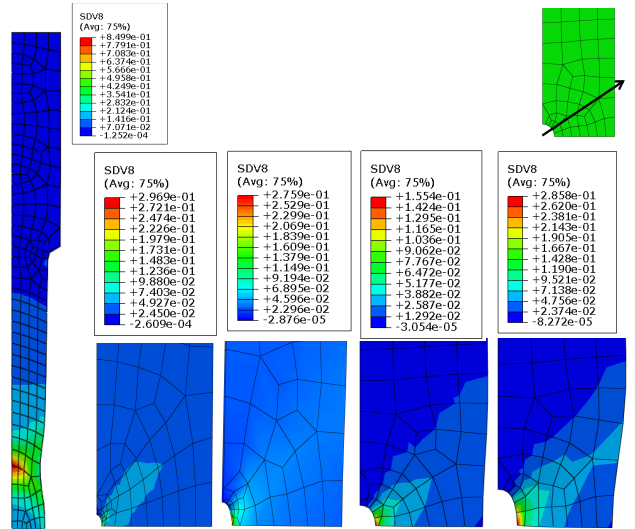


Figure 19: Longitudinal plastic strain distribution in the vicinity of the hole for different hole sizes, mild steel

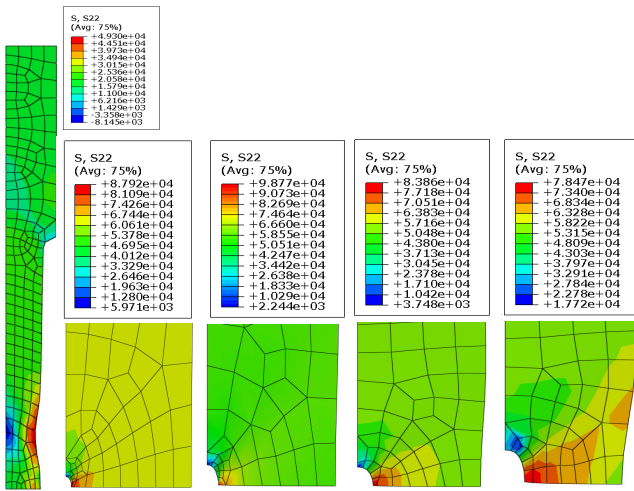


Figure 20: Longitudinal stress distribution in the vicinity of the hole for different hole sizes, mild steel

The stress distribution before cracking and the crack extension path of the perforated cast iron specimens are shown in figures 21 and 22 which illustrate the finite element results using the damage model and XFEM in Abaqus.

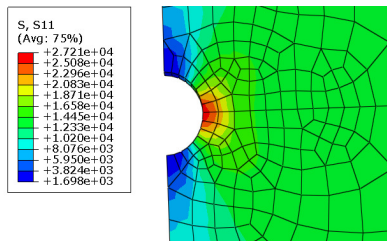


Figure 21: Longitudinal stress distribution for cast iron prior to crack

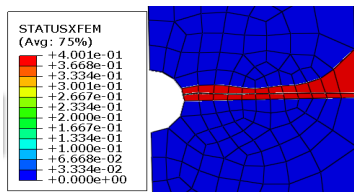


Figure 22: Crack propagation path for cast iron specimen

The longitudinal stress redistribution during the crack propagation for the cast iron specimen in the failure ligament is depicted in figure 23.

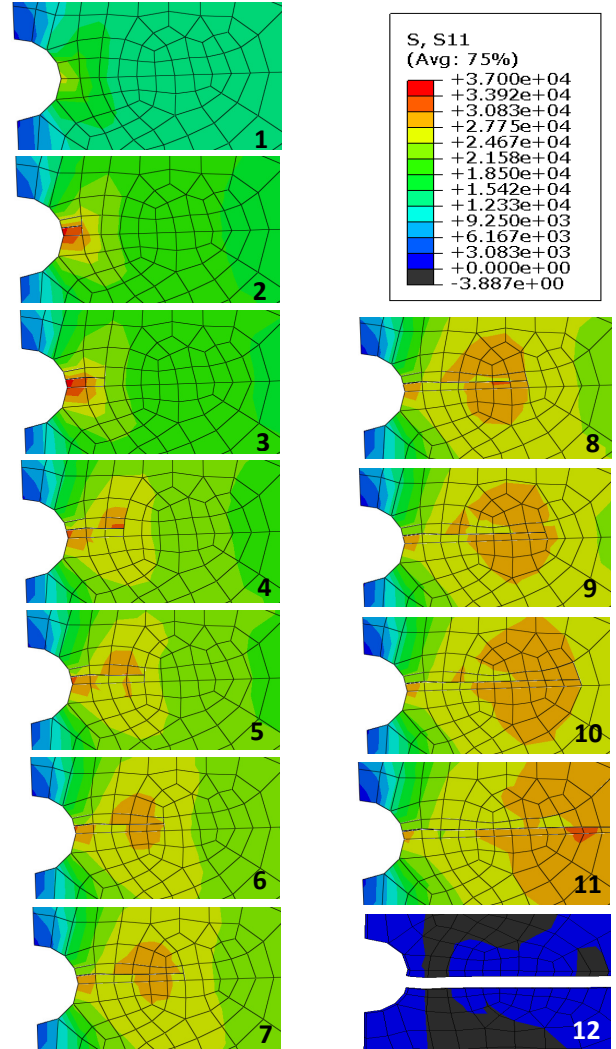


Figure 23: Stress redistribution during the crack propagation, cast iron

Figure 23 shows that the stress concentration zone is moving along the crack path behind the crack tip. The non zero value of the stress in the cracked region is due to the presence of the cohesive zone which infers that the two separated parts are still connected until the crack reaches the other edge of the specimen. Finally at the final stage when the flat bar is separated into two parts, the axial surface tractions become zero at the crack surfaces.

4 CONCLUDING REMARKS

The effect of stress concentrations in plates with circular perforations is discussed. Kirsch's paper is reviewed and his experiments for mild steel and cast iron are discussed and visualized. Although a factor two to three reduction in load capacity is expected, the reduction of perforated specimens is considerably less than fifteen percent and exceeds in some cases the capacity of unperforated bars. To understand this puzzling behavior a set of experiments for mild steel and cast iron are presented and discussed. It was confirmed that the reduction of the ultimate load capacity of cast iron is far less than 1/3 in accordance with the experimental results of Kirsch.

The DIC results showed that the localized plastic zones were present at the edge of the circular perforations for cast iron, figure 24, which reduced the stress concentration and increased the ultimate load capacity of the cast iron specimen to nearly 90% of the unperforated specimens.

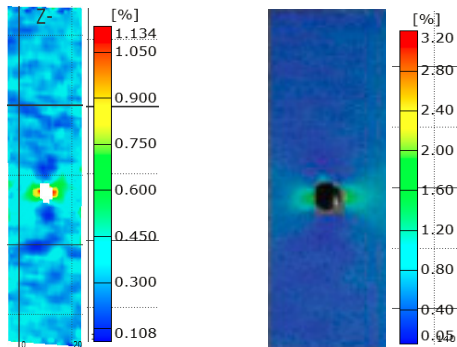


Figure 24: Localized plastic zones on cast iron specimens

In the case of mild steel, the elastoplastic FE model, localization analysis and DIC results all confirmed the experimental observations and the formation of shear bands and active plas-

tic deformations involved in reducing the stress concentration effect and maintaining if not exceeding the ultimate load capacity of the unperforated bars.

REFERENCES

- [1] Kirsch, G., 1898. Die Theorie der Elastizität und die Beduerfnisse der Festigkeitslehre. *Zeitschrift des Vereins Deutscher Ingenieure*, **32**:797–807
- [2] Willam, K. and Iordache, M. M., 1996. Computational simulation of discontinuous failure processes. *Mecanica computacional*, **17**:227–242
- [3] Steinmann, P. and Willam, K., 1994. Finite-Element analysis of elastoplastic discontinuities. *Journal of engineering mechanics*. **120**:2428–2442
- [4] Inglis, C.E., 1913. Stresses in a plate due to presence of cracks and sharp corners. *Transaction of the institute of naval architects*, **50**:219–241
- [5] Borelli, A. P. and Chong, K. P., 2000. *Elasticity in engineering mechanics*. 2nd ed. New York, Wiley-Interscience.
- [6] Anderson, T. L., 1991. *Fracture mechanics: fundamentals and applications*. CRC Press.
- [7] Giner, E., Sukumar, N., Tarancón, J.E. and Fuenmayor, F.J. 2009. An Abaqus implementation of the extended finite element method. *Engineering Fracture Mechanics*, **76**:347–368
- [8] Moës, N., Dolbow, J. and Belytschko, T. 1999. A finite element method for crack growth without remeshing. *International journal for numerical methods in engineering*, **46**:131–150